Zinc as chaperone-mimicking agent for retardation of amyloid β peptide fibril formation

Axel Abelein, Astrid Gräslund, and Jens Danielsson[1]

Department of Biochemistry and Biophysics, Stockholm University, 106 91 Stockholm, Sweden

Edited by Christopher M. Dobson, University of Cambridge, Cambridge, United Kingdom, and approved February 23, 2015 (received for review November 17, 2014)

Metal ions have emerged to play a key role in the aggregation process of amyloid β (Aβ) peptide that is closely related to the pathogenesis of Alzheimer's disease. A detailed understanding of the underlying mechanistic process of peptide–metal interactions, however, has been challenging to obtain. By applying a combination of NMR relaxation dispersion and fluorescence kinetics methods we have investigated quantitatively the thermodynamic Aβ–Zn^{2+} binding features as well as how Zn^{2+} modulates the nucleation mechanism of the aggregation process. Our results show that, under near-physiological conditions, substoichiometric amounts of Zn^{2+} effectively retard the generation of amyloid fibrils. A global kinetic profile analysis reveals that in the absence of zinc $Aβ_{40}$ aggregation is driven by a monomer-dependent secondary nucleation process in addition to fibril-end elongation. In the presence of Zn^{2+}, the elongation rate is reduced, resulting in reduction of the aggregation rate, but not a complete inhibition of amyloid formation. We show that Zn^{2+} transiently binds to residues in the N terminus of the monomeric peptide. A thermodynamic analysis supports a model where the N terminus is folded around the Zn^{2+} ion, forming a marginally stable, short-lived folded $Aβ_{40}$ species. This conformation is highly dynamic and only a few percent of the peptide molecules adopt this structure at any given time point. Our findings suggest that the folded $Aβ_{40}$–Zn^{2+} complex modulates the fibril ends, where elongation takes place, which efficiently retards fibril formation. In this conceptual framework we propose that zinc adopts the role of a minimal antiaggregation chaperone for $Aβ_{40}$.

Alzheimer's disease | amyloid beta peptide | aggregation kinetics | zinc ion interactions | NMR relaxation

Neurodegenerative disorders, such as Alzheimer's disease (AD), have their origin in protein misfolding and generation of amyloid aggregates that have been shown to mediate toxic effects on neurons (1, 2). The aggregation of the amyloid β (Aβ) peptide is closely linked to the pathogenesis of AD (3) and is strongly dependent on environmental conditions. Metal ions have been suggested to play a key role in AD pathogenesis (4, 5), and they have been suggested to be involved in generation of amyloid and modulation of cytotoxicity (6, 7). It seems that Zn^{2+} ions have a protective effect on Aβ's toxicity, at low Zn^{2+} concentrations, whereas higher concentrations may enhance toxicity (8, 9). To this date, it is unclear how the Zn^{2+} levels are altered in the AD brain, and seemingly contradictory studies have reported both elevated and decreased zinc levels (ref. 5 and references therein). In particular, zinc and copper ions have, however, been observed to be enriched in the amyloid plaques from brain tissues of AD patients (i.e., metal ions seem to coaggregate with Aβ) (4, 10, 11).

In in vitro studies, Zn^{2+} has been reported to inhibit formation of amyloid fibrils at a metal:peptide ratio of 2:1 (7). However, at high Zn^{2+} concentration it is suggested that amorphous aggregates are formed (12–14). Structural NMR studies on Aβ–Zn^{2+} interactions showed that Zn^{2+} binds to the N terminus of the 40-residue variant of Aβ ($Aβ_{40}$) (15–17) where the first 16 residues are the minimal peptide sequence for Zn^{2+} binding (16). In $Aβ_{40}$ the Zn^{2+} ion is coordinated by four ligands, the histidines H6, H13, and H14 and the N-terminal D1 (15). Interaction between Zn^{2+} and $Aβ_{40}$ causes NMR signal loss of the N-terminal residues (15, 17), and these data suggest that NMR signal loss may be attributed to a chemical exchange process on an NMR intermediate time scale (18) as reported for similar exchanging systems (19–21).

In general, modulation of amyloid aggregation by potential inhibitors may occur through interactions with monomers, oligomeric and/or fibrillar species that influence primary and secondary nucleation reactions and/or fibril-end elongation (22, 23). With a kinetic analysis of aggregation profiles the dominating microscopic aggregation mechanism can be determined (24–26). This approach can be applied to characterize which microscopic event(s) during primary and/or secondary pathway is(are) prevented by an inhibitor (23).

Despite the huge numbers of studies of the interaction between $Aβ_{40}$ and metals, and the subsequent effect on self-assembly and aggregation, no detailed model for the molecular mechanism of the modulation of fibril formation has been proposed. Here, we analyze $Aβ_{40}$ aggregation kinetics in the absence and presence of substoichiometric concentrations of Zn^{2+} ions to elucidate at which level and which microscopic rate constant(s) is(are) modulated by Zn^{2+}. In addition, we use NMR spectroscopy to follow the details of the zinc binding and folding of $Aβ_{40}$ around the zinc ion.

Results and Discussion

One fundamental characteristic property of $Aβ_{40}$ is the self-assembly into insoluble aggregates under both quiescent and agitated conditions, subsequently resulting in formation of mature amyloid fibrils. The aggregation kinetics (i.e., the time dependence of protein aggregate formation) is strongly dependent on the experimental conditions such as pH, ionic strength, and temperature. Under carefully monitored conditions, however, reproducible kinetics can be achieved (27). Similar to other

Significance

One histologic hallmark of Alzheimer's disease is the self-assembly of amyloid β peptide (Aβ) into insoluble amyloid aggregates. This aggregation process is strongly dependent on environmental conditions and metal ions, such as zinc, have been shown to modulate Aβ aggregation. To understand the underlying molecular mechanism of how zinc affects fibril formation we analyzed the aggregation kinetics and could conclude that zinc causes a significant reduction in elongation rate (i.e., monomer addition to the fibril ends). We used NMR methods to elucidate the details of zinc binding and we found that the N terminus of Aβ transiently folds around the zinc ion, forming a metastable dynamic complex.

Author contributions: A.A., A.G., and J.D. designed research; A.A. and J.D. performed research; A.A. and J.D. analyzed data; and A.A., A.G., and J.D. wrote the paper.

The authors declare no conflict of interest.

This article is a PNAS Direct Submission.

See Commentary on page 5267.

[1]To whom correspondence should be addressed. Email: jensd@dbb.su.se.

This article contains supporting information online at www.pnas.org/lookup/suppl/doi:10.1073/pnas.1421961112/-/DCSupplemental.

amyloid-forming proteins, $A\beta_{40}$ aggregation kinetics generally displays a sigmoidal pattern (28), and the aggregation kinetics is fully described by two phenomenological parameters $\tau_{1/2}$ and r_{max}, where $\tau_{1/2}$ is the time for depletion of half of the monomer pool by aggregation and r_{max} is the maximum growth rate (*Supporting Information*). Under dilute conditions at near-physiological pH (~7.2–7.4) $A\beta_{40}$ alone reveals aggregation traces that fit well to this simple sigmoidal behavior under quiescent conditions (Fig. 1*A*). This is in line with earlier findings for both $A\beta_{40}$ and the 42-residue-long variant $A\beta_{42}$ (27). To test the effect of substoichiometric concentrations of zinc on $A\beta_{40}$ aggregation we measured the aggregation kinetics in the presence of Zn^{2+}. Furthermore, to characterize the quantitative effect of Zn^{2+}, we determined the aggregation parameters at various zinc concentrations ranging from 0.5 to 2.5 μM at constant $A\beta_{40}$ concentration (20 μM) (Fig. 2*A*).

Effect of Zinc Ions on $A\beta_{40}$ Aggregation. The kinetic parameter $\tau_{1/2}$ is exponentially dependent on Zn^{2+} concentration (Fig. 2*B*), with an effective retardation of thioflavin T (ThT)-detected amyloid formation. The $\tau_{1/2}$ dependence on Zn^{2+} concentration, at constant $A\beta_{40}$ concentration, is given by $\tau_{1/2} = \tau_0 \cdot \exp([Zn^{2+}]/c_e)$, where $\tau_0 = 14.9 \pm 0.6$ h describes the aggregation half time without zinc ions and $c_e = 3.1 \pm 0.2$ μM is the Zn^{2+} concentration that prolongs $\tau_{1/2}$ by a factor e. A similar pattern has been observed for Cu^{2+}-induced inhibition of $A\beta_{42}$ aggregation (29). The final concentration of aggregates as well as the fibril morphology in the concentration range of 0–2.5 μM Zn^{2+} is about the same, as monitored by the ThT end-point fluorescence (Fig. 2*C*) and FTIR spectroscopy (Fig. S1), suggesting that Zn^{2+} prolongs the amyloid formation rather than fully inhibits the production of the final amyloid species, and this in turn indicates that Zn^{2+} interferes with the kinetic buildup of the aggregates.

To obtain further insight into the microscopic events that underlie the macroscopic inhibition of aggregation kinetics we studied the zinc-induced effects on $A\beta_{40}$ aggregation in more detail.

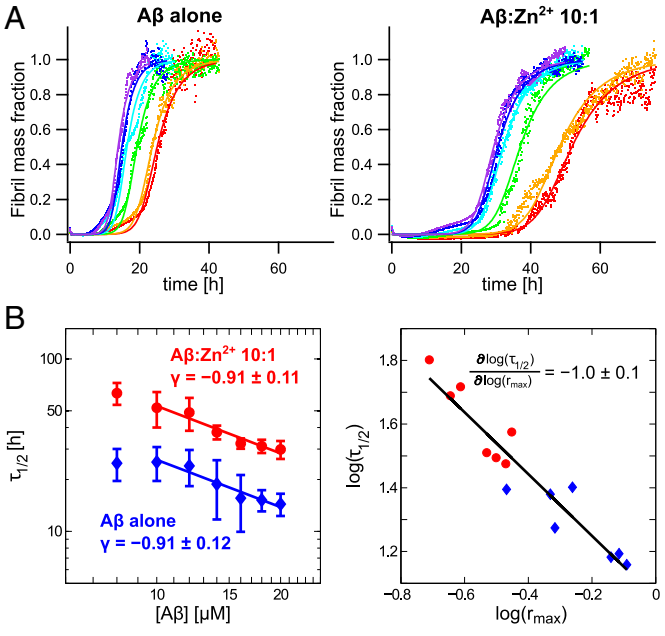

Fig. 1. (*A*) Aggregation kinetics of $A\beta_{40}$ alone (*Left*) and $A\beta_{40}$:Zn^{2+} 10:1 (*Right*) at different peptide concentrations with global fits of normalized aggregation traces of 10 (red), 12 (orange), 14 (green), 16 (cyan), 18 (blue), and 20 (violet) μM $A\beta_{40}$. (*B*) Variance weighted mean $\tau_{1/2}$ values, with and without Zn^{2+}, exhibit the same half-time exponent γ (*Left*). The correlation plot of the fitting parameters $\log(\tau_{1/2})$ vs. $\log(r_{max})$ features a slope of -1.0 ± 0.1 with $R^2 = 0.90$ (*Right*).

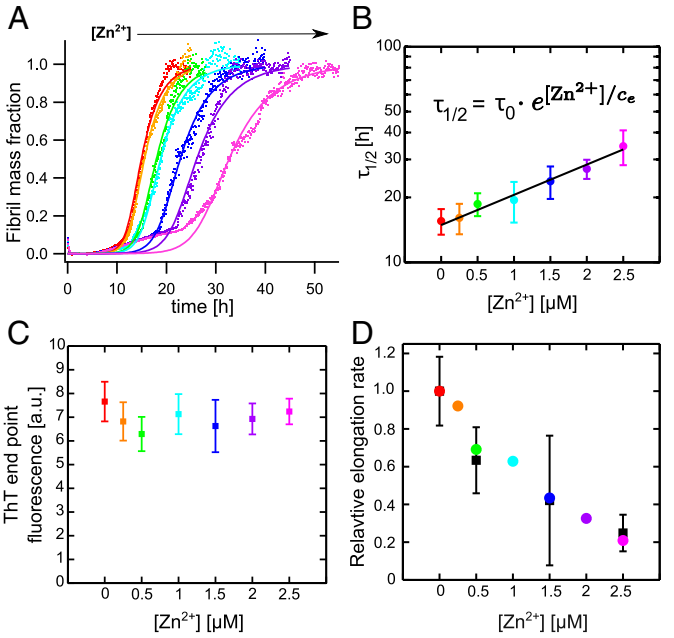

Fig. 2. (*A*) Aggregation traces of 20 μM $A\beta_{40}$ with different Zn^{2+} concentrations were globally fitted with $\sqrt{k_+ k_2}$ as a free parameter whereas $\sqrt{k_n/k_2}$ was constrained for all $[Zn^{2+}]$. (*B*) Mean $\tau_{1/2}$ values show an exponential $[Zn^{2+}]$ dependence: $\tau_{1/2} = \tau_0 \cdot \exp([Zn^{2+}]/c_e)$. (*C*) ThT end-point fluorescence at different $[Zn^{2+}]$. (*D*) The relative elongation rate from the global fit analysis displayed in *A* (colored points), with k_+ as the sole free fitting parameter, and elongation rates determined as the initial slopes (black squares) from preseeded aggregation kinetics.

Zinc Ions and $A\beta_{40}$ Nucleation. $A\beta_{40}$ aggregation has been studied in great detail and can in general be described by a number of microscopic rate constants related to primary nucleation events of order n_c (k_n) and secondary pathways including elongation at the fibril ends (k_+), fragmentation of formed fibrils (k_-) and secondary nucleation catalyzed on the surface of formed fibrils characterized by the reaction order n_2 (k_2) (24, 26). Under quiescent conditions fragmentation has been shown to be negligible (30), whereas under agitating conditions fragmentation has an important contribution (25, 27).

To distinguish between primary and secondary pathways we followed the protocol suggested by Cohen et al. (24) and performed kinetic aggregation experiments where $A\beta_{40}$ samples were preseeded with $A\beta_{40}$ aggregates (*Supporting Information* and Figs. S2 and S3). Both seeded $A\beta_{40}$ alone and seeded $A\beta_{40}$ in the presence of Zn^{2+} at molar equivalents of 10:1 $A\beta_{40}$:Zn^{2+} show sigmoidal aggregation traces. Aggregation of seeded $A\beta_{40}$ alone reached its final saturation phase within the lag time of unseeded $A\beta_{40}$ (Fig. S3). This indicates that $A\beta_{40}$ aggregation is completely dominated by secondary nucleation pathways. This is in agreement with findings for $A\beta_{42}$ (25).

Although the $\tau_{1/2}$ values are significantly longer for $A\beta_{40}$ in the presence of Zn^{2+}, the aggregation is again fully leveled out within the lag-time of unseeded $A\beta_{40}$, and thus the secondary pathway process dominates also in the presence of Zn^{2+} (Fig. S3). Taken together, we conclude that Zn^{2+} does not directly affect primary nucleation, but slows down the secondary pathway aggregation and thereby delays growth of amyloid fibril material.

Microscopic Rate Constants of $A\beta_{40}$ Aggregation, With and Without Zinc. To further characterize how zinc affects the secondary nucleation pathways we studied how the aggregation kinetics depends on the initial $A\beta_{40}$ monomer concentration, $m(0)$. The kinetic parameter $\tau_{1/2}$, which is correlated to the lag time, is dependent

on $m(0)$, and can be fitted to a power law $\tau_{1/2} \propto m(0)^{\gamma}$ (26, 27) (Fig. 1*B* and *Supporting Information*). A completely monomer-independent secondary nucleation pathway where this step is saturated, that is, where increasing the available monomers does not increase the rate, is characterized by a half-time exponent of $\gamma = -0.5$, whereas a fully monomer-dependent process with a secondary reaction order of $n_2 = 2$ yields a value of $\gamma = -(n_2 + 1)/2 = -1.5$ (24, 26). $A\beta_{40}$ alone has been shown to cover γ values from −1.5 at very low concentration to −0.2 at concentrations well above the saturation limit (30).

Here, we found that, in the concentration interval 10–20 μM $A\beta_{40}$, $\gamma = -0.9 \pm 0.1$ in absence of seeds (Fig. 1*B*). This concentration dependence is unaffected by the presence of Zn^{2+}, and the $\tau_{1/2}$ values again feature a half-time exponent of -0.9 ± 0.1. We conclude that the dominating aggregation mechanisms are unaffected by zinc, compared with $A\beta_{40}$ alone, but the microscopic rate constants defining the kinetics are reduced. Furthermore, for an aggregation mechanism dominated by secondary aggregation pathways rather than by primary nucleation, the aggregation parameters $\tau_{1/2}$ and r_{max} are interdependent (24) under steady-state conditions. Here, we investigated data at various $A\beta_{40}$ concentrations with and without Zn^{2+} and found a good correlation between $\log(\tau_{1/2})$ and $\log(r_{max})$ with slope -1.0 ± 0.1. In addition, the data derived from $A\beta_{40}$ alone and with Zn^{2+} cluster separately but on the same line, again suggesting a common aggregation mechanism (Fig. 1*B*) but with slower kinetics in the presence of Zn^{2+}.

Global Analysis of Aggregation Kinetics. To obtain further information on which aggregation step is primarily affected by zinc ions, we used all kinetic traces at various $A\beta_{40}$ concentrations and fitted them globally to the kinetic model proposed by Meisl et al. (30) (*Supporting Information*). From this fit we obtained combinations of the rate constants, $\sqrt{k_+ k_n}$ related to primary nucleation and elongation and $\sqrt{k_+ k_2}$ related to secondary nucleation and elongation and in addition K_M, the Michaelis constant for saturation of secondary nucleation. The global fits were performed using $n_c = n_2 = 2$ for the reaction orders for primary and secondary nucleation (30) (*Supporting Information*).

From the global fit of $A\beta_{40}$ alone the saturation constant was determined to 15 ± 3 μM and we could validate this by calculating $\sqrt{K_M}$ from the experimentally determined γ, which depends only on n_2, $m(0)$, and K_M, and we found $\sqrt{K_M} = 12.5 \pm 1.5$ μM (*Supporting Information*), in good agreement with the global fit analysis. The kinetic parameters determined from global fitting are listed in Table S1. The effect of zinc ions on one single nucleation rate can be estimated by fixing one global fit parameter across all Zn^{2+} concentrations and allowing the other one to vary, which is then the only effective free-fit parameter (*Supporting Information*). With this analysis, we found that individually changing k_2 and k_+ could explain the observed retardation of aggregation, whereas varying k_n alone is not sufficient to capture the observed effect on the aggregation traces (Fig. 2*A* and Fig. S4). Notably, the value of K_M is basically not changed upon addition of zinc, which suggests that k_2 is less likely to be affected (*Supporting Information*). To further distinguish whether k_2 or k_+ is the primary determinant of aggregation reduction we performed aggregation experiments with highly preseeded samples. Owing to the high number of added aggregates the initial growth rate basically stems entirely from elongation (24). We found that the initial slopes of preseeded samples follow the same trend as obtained from the global fit analysis when selecting k_+ as the sole effective free-fit parameter (Fig. 2*D*). Thus, a reductionist model, where primarily the elongation rate is affected by zinc, explains surprisingly well the observed aggregation kinetics.

The zinc-induced retardation in elongation rate is in fact in the same regime, or even more efficient, as that found for the specific chaperone Ssa1p inhibition of the prion protein Ure2p aggregation in yeast cells (31). Although the effects on the microscopic rates suggest that Zn^{2+} results in reduction in fibril elongation rate no molecular mechanism is revealed from the aggregation kinetic studies. To obtain further insight in the detailed molecular mechanisms we used NMR to study the dynamic interaction between $A\beta_{40}$ and zinc ions.

Monomeric $A\beta_{40}$ and Zn^{2+} Interaction. At near-physiological conditions $A\beta_{40}$ features a well-resolved ^1H-^{15}N heteronuclear single quantum coherence (HSQC) NMR spectrum (15, 32). Titration of Zn^{2+} onto $A\beta_{40}$, however, results in significant NMR signal intensity attenuation on the first 16–18 residues (Fig. S5*A*), as previously reported by us and others (15–17). The signal intensity of the C-terminal residues remains basically unaffected (Fig. S5*A*). Notably, the sample is relatively stable for a time period of ∼10 d and over a temperature interval of 278–290 K and only minor general NMR signal loss was observed (Fig. S5*A*). Hence, although a very slow aggregation process seems to be present, the sample stability enabled us to perform long-acquisition NMR experiments. This slow aggregation stands in contrast to the much faster aggregation described above (Fig. 1*A*) and is due to the fact that the NMR experiments are conducted at a much lower temperature.

Folding of $A\beta_{40}$ Around a Zinc Ion. The loss of signal intensity has been assigned to chemical exchange on an intermediate timescale (15, 17). The fact that the signal attenuation does not only affect the Zn^{2+} ligands (D1, H6, H13, and H14) indicates a regional conformational change of $A\beta_{40}$ upon Zn^{2+} binding, involving the first 16–18 residues. Thus, the primary zinc binding does not seem to cause the observed line broadening, but rather the induced folding of the N terminus to align the zinc ligands. This folded state can be assumed to be more compact than the disordered free peptide and would directly be reflected in the hydrodynamic radius, R_H. An alternative interpretation to the signal attenuation is the putative transient formation of higher-order aggregates owing to zinc binding, similar to the formation of transient higher-order coaggregates between $A\beta_{40}$ and lacmoid (20) and the surfactants sodium/lithium dodecyl sulfate (SDS/LiDS) (21). However, this would typically affect all residues, because the relaxation properties of all residues would change upon formation of a larger complex (20). In addition, R_H would increase upon Zn^{2+} interaction.

To test the hypothesis with a more compact zinc bound state we performed NMR pulsed field gradient diffusion measurements on 75 μM $A\beta_{40}$ alone and in the presence of 20 and 40 μM Zn^{2+}. The results show that the translational diffusion coefficient indeed increases with increasing Zn^{2+} concentration (Fig. 3*A*). This translates to a more compact structure when Zn^{2+} is bound to the peptide. R_H for the free peptide under these conditions is 16.6 Å, in good agreement with earlier findings (33), and decreases monotonically to 15.9 Å at 40 μM Zn^{2+}. The increased compactness of $A\beta_{40}$ in the zinc bound state supports the assumption that the signal attenuation is due to transient folding of monomeric $A\beta_{40}$, rather than transient formation of larger complexes. Furthermore, to ensure that monomeric $A\beta_{40}$ binds Zn^{2+}, we used LiDS micelles where the zinc-binding N terminus of monomeric $A\beta_{40}$ is solvent-accessible and outside the micelles (34), and we observed a very similar binding pattern as for free $A\beta_{40}$ in aqueous solution (*Supporting Information* and Fig. S5*D*). From these findings we conclude that Zn^{2+} binds to monomeric soluble $A\beta_{40}$ and induces an N-terminal fold of the peptide around the zinc ion.

Chemical Exchange Between Zinc-Bound and Free $A\beta_{40}$. To elucidate the reasons for the NMR signal attenuation upon Zn^{2+} binding we applied ^{15}N Carr–Purcell–Meiboom–Gill (CPMG) relaxation dispersion measurements (18, 35). These experiments allow detection of exchange rates typically in the microsecond-to-millisecond range.

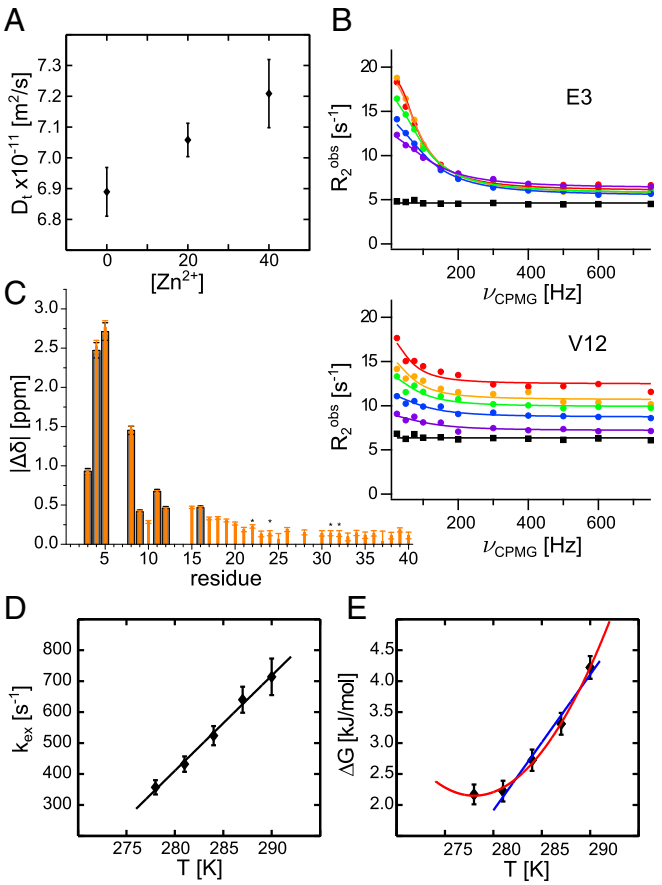

Fig. 3. (*A*) Translational diffusion coefficient, D_t, of 75 μM Aβ$_{40}$ alone and in the presence of 20 and 40 μM Zn^{2+} at 281 K (error bars: SD of five or more measurements). (*B*) Relaxation dispersion profiles of selected residues for 75 μM Aβ in the presence of 20 μM Zn^{2+} (circles) at 278 (red), 281 (orange), 284 (green), 287 (blue), and 290 K (violet) and Aβ alone at 281 K (black squares). (*C* and *D*) The fitting parameters absolute chemical shift differences $|\Delta\delta|$ and exchange rate k_{ex} from the global fit. Chemical shift differences were constrained to the same values for all temperatures and fitted for all (orange) and only the eight residues with significant relaxation dispersion amplitudes (gray). The stars mark signals with overlap in the spectrum. (*E*) The Gibbs free energy, obtained from the zinc-bound folded population, p_B, fitted to Eq. **1** (red). For higher temperature the Gibbs free energy is also fitted to $\Delta G(T) = \Delta H^0 - T\Delta S^0$ (blue). Error bars in *C*–*E* were estimated from fitting errors.

The slow aggregation process occurs on a timescale of days under the present conditions, which is observable by the overall minor signal loss (<25%), and occurs on a completely different timescale, and hence its effect on the exchange rates is assumed to be negligible.

The relaxation dispersion experiments were performed on 75 μM ^{15}N-Aβ$_{40}$ with 20 μM Zn^{2+} at five different temperatures between 278–290 K. Residues that show significant relaxation dispersion profiles are found exclusively in the N terminus where eight residues feature high-amplitude profiles (Fig. 3 *B* and *C* and Fig. S6). In this temperature interval the relaxation dispersion profiles show subtle but significant temperature dependence (Fig. 3*B*). In contrast, Aβ$_{40}$ alone does not display any significant relaxation dispersion profiles, underlining that the chemical exchange stems from zinc interactions.

Applying a global fit analysis, including all residues displaying significant dispersion profiles, the temperature-dependent relaxation dispersion data (*Supporting Information*) fits to a two-state model consisting of a state that can be assigned to free peptide and a Zn^{2+}-bound folded state. The exchange rate k_{ex} between the two states as well as the population of the zinc-bound folded state p_B were fitted globally, and the relaxation rates, R_2^0, and the magnitude of the chemical shift differences between the states, $|\Delta\delta_N|$, are residue-specific fitting parameters. $|\Delta\delta_N|$ was constrained to the same values for all temperatures and Zn^{2+} concentrations, thus assuming the bound state to be the same at all temperatures in the interval. The results from the global fit are summarized in Table 1, Fig. 3 *B*–*D*, and *Supporting Information*.

The eight residues that show high-amplitude relaxation dispersion profiles exhibit chemical shift changes $|\Delta\delta_N|$ in the interval 0.4–2.7 ppm (Fig. 3*C*). As expected, the exchange rate, k_{ex}, increases with temperature from 360 s^{-1} at 278 K to 715 s^{-1} at 290 K (Fig. 3*D*) and shows a linear dependence with a slope of 30.7 ± 1.5 s^{-1}K^{-1}. The expected exchange rate can thus be extrapolated to physiological temperature, 310 K, and the extrapolated exchange rate is 1,300 s^{-1}. Also, the population of zinc-bound folded Aβ$_{40}$ is temperature-dependent and decreases from 6.7 to 3.5% when the temperature is increased from 278 to 290 K. Notably, when all temperatures are considered the population p_B does not follow a linear temperature dependence, which would be expected if the binding enthalpy and entropy exhibit nonnegligible temperature dependence. The curvature is expected from protein folding theory owing to differences in the heat capacity of folded and unfolded states (36).

Rate-Limiting Step in Aβ$_{40}$–Zinc Interaction. Using the population determined from the relaxation dispersion experiments an apparent dissociation constant, K_D^{app}, for zinc binding to Aβ$_{40}$ can be determined. This assumes that primary 1:1 zinc binding is the rate-limiting step in this reaction (*Supporting Information*). Here, K_D^{app} was found to be 470 μM at 290 K, significantly different from 6.6 μM determined by fluorescence under similar conditions (15). To validate these findings and to resolve this apparent contradiction we used the diffusion data (Fig. 3*A* and *Supporting Information*) to estimate K_D^{app} to ∼210 μM at 281 K in the presence of 40 μM Zn^{2+}. This estimation is thus in very good agreement with the $K_D^{app} = 210 \pm 20$ μM at 281 K determined by relaxation dispersion experiments (Table 1).

The significantly weaker K_D^{app} for the overall process compared with primary zinc binding again indicates that the NMR-observed process is folding around the Zn^{2+} ion, and that this is the rate-limiting step in this process. A scheme for such reaction can be written as

$$A\beta_{40} + Zn^{2+} \underset{k_{off}}{\overset{k_{on}}{\rightleftharpoons}} A\beta_{40}Zn^{2+}(U) \underset{k_U}{\overset{k_F}{\rightleftharpoons}} A\beta_{40}Zn^{2+}(F).$$

Here, Aβ$_{40}$Zn^{2+} (U) is the zinc-bound unfolded state and the folded state, Aβ$_{40}$Zn^{2+} (F), is formed by the folding rate k_F, and

Table 1. Global fit parameters p_B and k_{ex}, apparent dissociation constant K_D^{app} (from Eq. S11) from a two-state model, and Gibbs free energy from a three-state model

Temperature, K	p_B, %	k_{ex}, s^{-1}	K_D^{app}, μM	$\Delta G^{U\to F}$, kJ/mol
20 μM Zn^{2+}				
278	6.7 ± 0.3	360 ± 25	210 ± 20	2.2 ± 0.2
281	6.7 ± 0.3	430 ± 30	210 ± 20	2.2 ± 0.2
284	5.7 ± 0.3	525 ± 35	260 ± 20	2.7 ± 0.2
287	4.8 ± 0.3	640 ± 45	330 ± 30	3.3 ± 0.2
290	3.5 ± 0.2	715 ± 60	470 ± 40	4.2 ± 0.2
10 μM Zn^{2+}				
281	3.2 ± 0.2	320 ± 30	230 ± 30	2.4 ± 0.2

Errors were determined from the fit.

the exchange rate is $k_{ex,Zn} = k_F + k_U$. To test this hypothesis we examined the Zn^{2+} concentration dependence on the population and exchange rate. Lowering the Zn^{2+} concentration from 20 to 10 μM is expected to result in a decrease of folded population by a factor of two whereas the exchange rate is expected only to exhibit weak concentration dependence. We found that the population decreased by 50% and k_{ex} only by 25% (Table 1 and Figs. S7 and S8), in line with the schematic model with $K_D \ll K_{eq} = k_U/k_F$; thus, zinc binds to the peptide with $K_D \sim 7$ μM and subsequently $A\beta_{40}$ folds in a rate-limiting step. The folded state was further characterized by the temperature dependence of the thermodynamic parameters derived from the relaxation dispersion experiments.

Thermodynamics of Zinc-Induced Folding of $A\beta_{40}$. The temperature dependence of the Zn^{2+} bound folded state p_B may be used to determine the folding reaction specific thermodynamic parameters (*Supporting Information*). As a first order of approximation we assume only a weak temperature dependence of the primary zinc binding with $K_D = 6.6$ μM (15), and used this to calculate the fraction folded $A\beta_{40}$, p_F, in relation to the zinc bound peptide p_{Zn}. The equilibrium constant K_{eq} of this reaction is given by the population of the folded state, $p_F = p_B$, $K_{eq} = p_B/(p_{Zn} - p_B)$, and the folding reaction is thermodynamically determined by the Gibbs free energy difference of the unfolded and the folded state $\Delta G^{U\to F}(T) = -RT \ln K_{eq}^{U\to F}(T)$. The free energy displays nonlinear temperature dependence (Fig. 3*E* and Fig. S9), as expected for protein folding (36). To account for the curved shape an explicit temperature dependence of $\Delta G(T)$ is introduced by the heat capacity $\Delta C_P = (\partial H/\partial T)_P$:

$$\Delta G(T) = \Delta H_{T_m} - T\Delta S_{T_m} + \Delta C_P(T - T_m) - T\Delta C_P \ln(T/T_m). \quad [1]$$

T_m refers to a reference temperature, which here is chosen as a melting temperature $T_m = \Delta H^0/\Delta S^0$. ΔH^0 and ΔS^0 are obtained from a first approximation fit for higher temperatures where $\Delta G(T)$ is linearly dependent on temperature $\Delta G(T) = \Delta H^0 - T\Delta S^0$. All determined parameters are given in Table 2. The negative signs of both ΔH^0 and ΔS^0 highlight the fact that zinc-induced folding of $A\beta_{40}$ is enthalpically favored yet entropically disfavored. Also, the nonzero heat capacity change generally monitors a solvation of polar groups (37). This implies that less peptide surface is exposed to solvent water in the folded state, in line with a zinc-induced folding of the N terminus of $A\beta_{40}$. The determined $\Delta C_P = -8.1 \pm 1.0$ kJ/K is relatively large and folding of $A\beta_{40}$ alone is expected to yield significantly lower ΔC_P (~−1.2 kJ/K) (38). This suggests that zinc binding per se and loss of coordinated water contribute to the determined ΔC_P. Furthermore, the curvature in $\Delta G^{U\to F}(T)$ results in that, when lowering the temperature, cold unfolding is induced already before the folded state is populated to more than 50%, that is, $\Delta G^{U\to F}(T) > 0$ for all temperatures and, thus, the folded state is only marginally stable. Extrapolating the free energy profile to 310 K the population folded $A\beta_{40}$–Zn^{2+} can be estimated to only 0.04%, highlighting that, at any given time point, only a very small fraction is folded. Still a large effect is found on the aggregation kinetics.

Table 2. Thermodynamic parameters from Fig. 3*E*

From $\Delta G(T) = \Delta H^0 - T\Delta S^0$		From Eq. 1 at $T_m = 271$ K	
ΔH^0	−60 ± 9 kJ/mol	ΔH_{T_m}	57 ± 13 kJ/mol
ΔS^0	−219 ± 30 J·mol^{-1}·K^{-1}	ΔS_{T_m}	199 ± 45 J·mol^{-1}·K^{-1}
		ΔC_P	−8.1 ± 1.0 kJ·mol^{-1}·K^{-1}

Errors were determined from the fit.

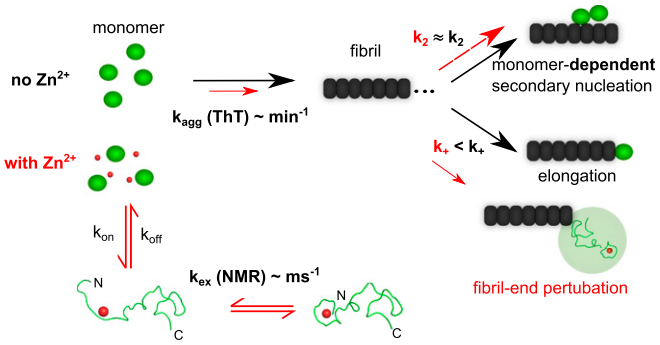

Fig. 4. $A\beta_{40}$ self-assembly follows a monomer-dependent secondary nucleation pathway and fibril formation is efficiently retarded in the presence of zinc ions by primarily inhibiting fibril-end elongation in a simplistic model. $A\beta_{40}$ in solution transiently forms a low-populated dynamic complex with Zn^{2+} where the peptide's N terminus is wrapped around the zinc ion. A simplistic mechanistic model is that Zn^{2+} inhibits elongation by modulation of the encounter complex between $A\beta_{40}$ and the fibril end.

Concluding Remarks

Taken together our findings can be summarized as an inhibition model where the normal aggregation pathway of $A\beta_{40}$ mainly is perturbed by a reduction in the elongation rate (Fig. 4). The very low concentration folded $A\beta_{40}$, at steady state, suggests that the observed effect is not due to a direct reduction of the effective $A\beta_{40}$ concentration by formation of a nonaggregating folded $A\beta_{40}$–Zn^{2+} complex, as found for natively folded proteins such as superoxide dismutase 1, where the folded state competes with the globally unfolded state that takes part in assembly and fibril elongation (39).

$A\beta_{40}$ aggregation has been suggested to be related to peptide reconfiguration time (40), and it may be pictured that after Zn^{2+} release the reconfiguration time of $A\beta_{40}$ is temporarily altered. However, such relatively unlikely reduced reconfiguration time is expected to affect both secondary nucleation and elongation rates.

Furthermore, the Zn^{2+} induced folding of $A\beta_{40}$ mainly affects the N terminus, which is normally assumed not to directly participate in amyloid formation and is not involved in the β-rich core of in vitro-produced $A\beta_{40}$ amyloid fibrils (41). In addition, binding of zinc reduces the net charge of the peptide from −3 to −1, thus consequently reducing electrostatic repulsion. This is expected to increase aggregation kinetic rates (39, 42), in stark contrast to our findings. However, at higher Zn^{2+} concentration, that is, under conditions when accelerated formation of amorphous aggregates was reported (12, 13), a suggested second weaker binding side, involving residues 23–28 (15), can be assumed to be more populated and electrostatic interaction may become the decisive factor for aggregation under these conditions.

Several molecular mechanisms could, individually or in combination, explain the observed reduction in elongation rate. A minimal model for fibril elongation must constitute two discrete steps where the monomer first binds to the fibril and forms an encounter complex (39) and subsequently folds on the fibril end to its tightly bound β-rich state (43). Modulation of the fibril ends by Zn^{2+} may cause perturbations of one or both steps, leading to retardation in aggregation kinetics. This also provides an explanation of why already very low relative concentrations of Zn^{2+} result in significant reduction in elongation rate, because the number of fibril ends is orders of magnitudes smaller than the number of free monomers.

The precise level of interaction and inhibition mechanism are yet to be determined, but we suggest two general mechanisms: (*i*) The zinc ion may exert strong binding to β-structured $A\beta_{40}$ at the end of the fibril, preventing further elongation by changing the local environment for peptide folding to the amyloid state,

and/or (*ii*) Zn^{2+}-induced folding of $A\beta_{40}$ modulates the strength of the encounter complex (i.e., $A\beta_{40}$ binds zinc during the lifetime of the encounter complex leading to a premature release of the peptide from the complex before it folds onto the fibril end) (Fig. 4). Our results showing that $A\beta_{40}$ binds Zn^{2+} with similar affinity and coordination also in complex with LiDS micelles underline the plausibility for such a mechanism.

Whether the findings in this study are transferable to the complex environment of the aging neuron remains to be investigated, but in a reductionist in vitro system the zinc ion could be assigned as a minimal efficient chaperone-mimicking agent for inhibition of $A\beta_{40}$ self-assembly and amyloid formation.

Materials and Methods

Recombinant $A\beta_{40}$ peptide was purchased from Alexo-Tech and samples were prepared as in ref. 32. Experiments were performed in 10 mM Hepes, pH 7.4, for NMR and 10 mM phosphate buffer, pH 7.2–7.4 for kinetics experiments, respectively. Zn^{2+} ions were added as chloride. ThT fluorescence aggregation kinetics experiments were performed at 37 °C under quiescent conditions using a 96-well plate. FTIR measurements were conducted at 4-cm^{-1} resolution on dried films obtained from ThT fluorescence end-point samples using an attenuated total reflection accessory. NMR experiments were acquired on a 700-MHz Bruker spectrometer equipped with a cryogenic probe. ^{15}N CPMG relaxation rates were recorded of 75 μM ^{15}N-$A\beta_{40}$ with 20 μM Zn^{2+} for five different temperatures from 278 to 290 K in steps of 3 K (same sample) as well as with 10 μM Zn^{2+} and without Zn^{2+} (different samples) both at 281 K using a CPMG pulse scheme (35) with a mixing time of 120 ms and 11 different delays between the 180° pulses as well as a reference experiment without the mixing period. Diffusion experiments were performed at 281 K in D_2O on three different samples without and with 20 and 40 μM Zn^{2+} using 16 different gradient strengths, a gradient pulse length of 3 ms, and a diffusion time of 100 ms. Detailed methods are described in *Supporting Information*.

ACKNOWLEDGMENTS. We thank Prof. Andreas Barth for helpful advice on FTIR. We acknowledge financial support by grants from the Swedish Research Council, the Swedish Brain Foundation, the Knut and Alice Wallenberg Foundation, and the Magn. Bergwall Foundation as well as access to the BioNMR Research Infrastructure.

1. Chiti F, Dobson CM (2006) Protein misfolding, functional amyloid, and human disease. *Annu Rev Biochem* 75:333–366.
2. Benilova I, De Strooper B (2011) An overlooked neurotoxic species in Alzheimer's disease. *Nat Neurosci* 14(8):949–950.
3. Haass C, Selkoe DJ (2007) Soluble protein oligomers in neurodegeneration: Lessons from the Alzheimer's amyloid beta-peptide. *Nat Rev Mol Cell Biol* 8(2):101–112.
4. Bush AI, et al. (1994) Rapid induction of Alzheimer A beta amyloid formation by zinc. *Science* 265(5177):1464–1467.
5. Ayton S, Lei P, Bush AI (2013) Metallostasis in Alzheimer's disease. *Free Radic Biol Med* 62:76–89.
6. Zatta P, Lucchini R, van Rensburg SJ, Taylor A (2003) The role of metals in neurodegenerative processes: Aluminum, manganese, and zinc. *Brain Res Bull* 62(1):15–28.
7. Yoshiike Y, et al. (2001) New insights on how metals disrupt amyloid beta-aggregation and their effects on amyloid-beta cytotoxicity. *J Biol Chem* 276(34):32293–32299.
8. Lovell MA, Xie C, Markesbery WR (1999) Protection against amyloid beta peptide toxicity by zinc. *Brain Res* 823(1-2):88–95.
9. Cardoso SM, Rego AC, Pereira C, Oliveira CR (2005) Protective effect of zinc on amyloid-beta 25-35 and 1-40 mediated toxicity. *Neurotox Res* 7(4):273–281.
10. Lovell MA, Robertson JD, Teesdale WJ, Campbell JL, Markesbery WR (1998) Copper, iron and zinc in Alzheimer's disease senile plaques. *J Neurol Sci* 158(1):47–52.
11. Miller LM, et al. (2006) Synchrotron-based infrared and X-ray imaging shows focalized accumulation of Cu and Zn co-localized with beta-amyloid deposits in Alzheimer's disease. *J Struct Biol* 155(1):30–37.
12. Tõugu V, et al. (2009) Zn(II)- and Cu(II)-induced non-fibrillar aggregates of amyloid-beta (1-42) peptide are transformed to amyloid fibrils, both spontaneously and under the influence of metal chelators. *J Neurochem* 110(6):1784–1795.
13. Ha C, Ryu J, Park CB (2007) Metal ions differentially influence the aggregation and deposition of Alzheimer's beta-amyloid on a solid template. *Biochemistry* 46(20):6118–6125.
14. Miller Y, Ma B, Nussinov R (2010) Zinc ions promote Alzheimer Abeta aggregation via population shift of polymorphic states. *Proc Natl Acad Sci USA* 107(21):9490–9495.
15. Danielsson J, Pierattelli R, Banci L, Gräslund A (2007) High-resolution NMR studies of the zinc-binding site of the Alzheimer's amyloid beta-peptide. *FEBS J* 274(1):46–59.
16. Minicozzi V, et al. (2008) Identifying the minimal copper- and zinc-binding site sequence in amyloid-beta peptides. *J Biol Chem* 283(16):10784–10792.
17. Rezaei-Ghaleh N, Giller K, Becker S, Zweckstetter M (2011) Effect of zinc binding on β-amyloid structure and dynamics: implications for Aβ aggregation. *Biophys J* 101(5):1202–1211.
18. Palmer AG, 3rd, Kroenke CD, Loria JP (2001) Nuclear magnetic resonance methods for quantifying microsecond-to-millisecond motions in biological macromolecules. *Methods Enzymol* 339:204–238.
19. Maltsev AS, Grishaev A, Bax A (2012) Monomeric α-synuclein binds Congo Red micelles in a disordered manner. *Biochemistry* 51(2):631–642.
20. Abelein A, Lang L, Lendel C, Gräslund A, Danielsson J (2012) Transient small molecule interactions kinetically modulate amyloid β peptide self-assembly. *FEBS Lett* 586(22):3991–3995.
21. Abelein A, et al. (2013) Formation of dynamic soluble surfactant-induced amyloid β peptide aggregation intermediates. *J Biol Chem* 288(32):23518–23528.
22. Härd T, Lendel C (2012) Inhibition of amyloid formation. *J Mol Biol* 421(4-5):441–465.
23. Arosio P, Vendruscolo M, Dobson CM, Knowles TPJ (2014) Chemical kinetics for drug discovery to combat protein aggregation diseases. *Trends Pharmacol Sci* 35(3):127–135.
24. Cohen SIA, Vendruscolo M, Dobson CM, Knowles TPJ (2012) From macroscopic measurements to microscopic mechanisms of protein aggregation. *J Mol Biol* 421(2-3):160–171.
25. Cohen SIA, et al. (2013) Proliferation of amyloid-β42 aggregates occurs through a secondary nucleation mechanism. *Proc Natl Acad Sci USA* 110(24):9758–9763.
26. Cohen SIA, et al. (2011) Nucleated polymerization with secondary pathways. I. Time evolution of the principal moments. *J Chem Phys* 135(6):065105.
27. Hellstrand E, Boland B, Walsh DM, Linse S (2010) Amyloid β-protein aggregation produces highly reproducible kinetic data and occurs by a two-phase process. *ACS Chem Neurosci* 1(1):13–18.
28. Biancalana M, Koide S (2010) Molecular mechanism of Thioflavin-T binding to amyloid fibrils. *Biochim Biophys Acta* 1804(7):1405–1412.
29. Mold M, Ouro-Gnao L, Wieckowski BM, Exley C (2013) Copper prevents amyloid-β(1-42) from forming amyloid fibrils under near-physiological conditions in vitro. *Sci Rep* 3:1256.
30. Meisl G, et al. (2014) Differences in nucleation behavior underlie the contrasting aggregation kinetics of the Aβ40 and Aβ42 peptides. *Proc Natl Acad Sci USA* 111(26):9384–9389.
31. Xu LQ, et al. (2013) Influence of specific HSP70 domains on fibril formation of the yeast prion protein Ure2. *Philos Trans R Soc Lond B Biol Sci* 368(1617):20110410.
32. Abelein A, Bolognesi B, Dobson CM, Gräslund A, Lendel C (2012) Hydrophobicity and conformational change as mechanistic determinants for nonspecific modulators of amyloid β self-assembly. *Biochemistry* 51(1):126–137.
33. Danielsson J, Jarvet J, Damberg P, Gräslund A (2002) Translational diffusion measured by PFG-NMR on full length and fragments of the Alzheimer Aβ (1-40) peptide. Determination of hydrodynamic radii of random coil peptides of varying length. *Magn Reson Chem* 40(13):S89–S97.
34. Jarvet J, Danielsson J, Damberg P, Oleszczuk M, Gräslund A (2007) Positioning of the Alzheimer Abeta(1-40) peptide in SDS micelles using NMR and paramagnetic probes. *J Biomol NMR* 39(1):63–72.
35. Tollinger M, Skrynnikov NR, Mulder FA, Forman-Kay JD, Kay LE (2001) Slow dynamics in folded and unfolded states of an SH3 domain. *J Am Chem Soc* 123(46):11341–11352.
36. Oliveberg M, Tan YJ, Fersht AR (1995) Negative activation enthalpies in the kinetics of protein folding. *Proc Natl Acad Sci USA* 92(19):8926–8929.
37. Prabhu NV, Sharp KA (2005) Heat capacity in proteins. *Annu Rev Phys Chem* 56:521–548.
38. Myers JK, Pace CN, Scholtz JM (1995) Denaturant m values and heat capacity changes: Relation to changes in accessible surface areas of protein unfolding. *Protein Sci* 4(10):2138–2148.
39. Lang L, Kurnik M, Danielsson J, Oliveberg M (2012) Fibrillation precursor of superoxide dismutase 1 revealed by gradual tuning of the protein-folding equilibrium. *Proc Natl Acad Sci USA* 109(44):17868–17873.
40. Acharya S, Lapidus LJ (2015) Reconfiguration of the Alzheimer's peptide kinetically controls aggregation in Alzheimer's disease. *Biophys J* 108(2):65a–66a.
41. Petkova AT, Yau WM, Tycko R (2006) Experimental constraints on quaternary structure in Alzheimer's beta-amyloid fibrils. *Biochemistry* 45(2):498–512.
42. Schreiber G, Haran G, Zhou HX (2009) Fundamental aspects of protein-protein association kinetics. *Chem Rev* 109(3):839–860.
43. Gurry T, Stultz CM (2014) Mechanism of amyloid-β fibril elongation. *Biochemistry* 53(44):6981–6991.